Alternating electron and proton transfer steps in photosynthetic water oxidation

André Klauss, Michael Haumann[1], and Holger Dau[1]

Physics Department, Freie Universität Berlin, 14195 Berlin, Germany

Edited by Harry B. Gray, California Institute of Technology, Pasadena, CA, and approved August 27, 2012 (received for review April 13, 2012)

Water oxidation by cyanobacteria, algae, and plants is pivotal in oxygenic photosynthesis, the process that powers life on Earth, and is the paradigm for engineering solar fuel–production systems. Each complete reaction cycle of photosynthetic water oxidation requires the removal of four electrons and four protons from the catalytic site, a manganese–calcium complex and its protein environment in photosystem II. In time-resolved photothermal beam deflection experiments, we monitored apparent volume changes of the photosystem II protein associated with charge creation by light-induced electron transfer (contraction) and charge-compensating proton relocation (expansion). Two previously invisible proton removal steps were detected, thereby filling two gaps in the basic reaction-cycle model of photosynthetic water oxidation. In the $S_2 \rightarrow S_3$ transition of the classical *S*-state cycle, an intermediate is formed by deprotonation clearly before electron transfer to the oxidant (Y_Z^{ox}). The rate-determining elementary step (τ, approximately 30 μs at 20 °C) in the long-distance proton relocation toward the protein–water interface is characterized by a high activation energy ($E_a = 0.46 \pm 0.05$ eV) and strong H/D kinetic isotope effect (approximately 6). The characteristics of a proton transfer step during the $S_0 \rightarrow S_1$ transition are similar (τ, approximately 100 μs; $E_a = 0.34 \pm 0.08$ eV; kinetic isotope effect, approximately 3); however, the proton removal from the Mn complex proceeds after electron transfer to Y_Z^{ox}. By discovery of the transient formation of two further intermediate states in the reaction cycle of photosynthetic water oxidation, a temporal sequence of strictly alternating removal of electrons and protons from the catalytic site is established.

In oxygenic photosynthesis, plants, algae, and cyanobacteria oxidize water at the manganese–calcium (Mn_4Ca) complex of photosystem II (PSII) (1–3). This process has shaped the atmosphere by massive O_2 formation (from water) and the biosphere by facilitating the large-scale production of primary biomass and energy-rich carbohydrates (4), but is still insufficiently understood. Improved insight into photosynthetic water oxidation could promote the development of biomimetic systems for direct production of solar fuels (3, 5–9).

In PSII, the absorption of a light quantum results in oxidation of a specific tyrosine (10), Y_Z [redox-active tyrosine residue (Tyr161) in the D1 subunit of PSII], which functions as the oxidant in the redox chemistry of water oxidation (9, 11, 12):

$$4 \bullet Y_Z^{ox} + 2\,H_2O \rightarrow 4 \bullet Y_Z^{red} + 4\,H^+ + O_2. \qquad [1]$$

The actual catalyst facilitating the reaction described by Eq. **1** is the Mn_4Ca complex bound to the proteins of PSII (13–15) (Fig. 1*A*). Four electrons are removed sequentially from the Mn complex [that is, the $Mn_4Ca(\mu\text{–}O)_n$ core and its ligand environment] by electron transfer to Y_Z^{ox}, resulting in accumulation of four oxidizing equivalents before the onset of O—O bond formation and O_2 liberation, as described by Kok's classical *S*-state cycle (16, 17) (Fig. 1*B*, inner circle of *S*-states). Four protons are removed by deprotonation of the Mn complex and relocation toward the aqueous phase of the thylakoid lumen (18–20).

The location of the Mn complex at the interface between the membrane-intrinsic part of PSII and the extrinsic lumenal proteins (13–15) (Fig. 1*A*) implies long-distance proton relocation toward the aqueous phase (approximately 30 Å), occurring within tens or hundreds of microseconds along chains of water molecules and ionic residues (21). The interrelation between electron transfer and protonation dynamics (that is, the relocation of protons on various time and length scales) is functionally crucial (1, 22–25). Our study aims to identify the basic sequence of electron transfer (ET) and long-distance proton relocation in the water oxidation cycle.

The electron transfer from the Mn complex to Y_Z^{ox} (22, 26–29) and the proton release (i.e., the appearance of protons in the aqueous phase) (18–20), have been investigated extensively. It was found (inter alia) that the observable proton release often does not reflect the removal of a proton from the Mn complex because electrostatically induced deprotonation of residues at the lumenal periphery of the protein masks the protein-intrinsic proton removal (20, 30). Nonetheless, it was possible to determine the "intrinsic proton release pattern" (i.e., the number of protons removed in each of the classical *S*-state transitions from the Mn complex), which is: 1 H^+ in $S_0 \rightarrow S_1$, 0 H^+ in $S_1 \rightarrow S_2$, 1 H^+ in $S_2 \rightarrow S_3$, and 2 H^+ in $S_3 \rightarrow S_0$ (18, 19, 31). The appearance of protons in the aqueous bulk phase rapidly after Y_Z^{ox} formation and prior to its reduction by ET from the Mn complex has been established firmly (19, 20, 30), but likely does not reflect the deprotonation of a chemical group (e.g., a substrate water molecule) at the Mn complex (18, 19, 31). This implies that the time-resolved detection of proton release into the aqueous phase cannot be employed to decide whether the proton removal from the Mn complex precedes the ET to Y_Z^{ox}.

The temporal sequence of electron and proton removal steps after rapid Y_Z^{ox} formation therefore has remained largely obscure, with one notable exception: Today there is strong experimental support that, after formation of the S_3 Y_Z^{ox} state in the $S_3 \rightarrow S_0$ transition, a proton is removed from the Mn complex before onset of the electron transfer to Y_Z^{ox} (22, 26, 32). This finding has led to an extension of the *S*-state cycle involving formation of a distinct S_4 state by deprotonation (inner circle of Fig. 1*B*) before S_4 formation by electron transfer (22, 17). Later, this reaction cycle was extended further to include each of the four protons (24, 33) (outer circle of Fig. 1*B*). However, the proposed sequence of events has remained hypothetical, in particular because the proton removal from the Mn complex in the $S_0^+ \rightarrow S_1^n$ and $S_2^+ \rightarrow S_2^n$ transitions could not be tracked in time-resolved experiments.

To detect proton removal from the Mn complex, we employ a photothermal beam deflection (PBD) experiment exploiting the high sensitivity of the PBD signal to density changes (34–38), which in the following are discussed in terms of apparent volume changes of the protein. Expansion and contraction of the PSII complex were monitored with microsecond resolution at a precision of

Author contributions: M.H. and H.D. designed research; A.K. performed research; A.K. analyzed data; and M.H. and H.D. wrote the paper.

The authors declare no conflict of interest.

This article is a PNAS Direct Submission.

[1]To whom correspondence may be addressed. E-mail: holger.dau@fu-berlin.de or michael.haumann@fu-berlin.de.

This article contains supporting information online at www.pnas.org/lookup/suppl/doi:10.1073/pnas.1206266109/-/DCSupplemental.

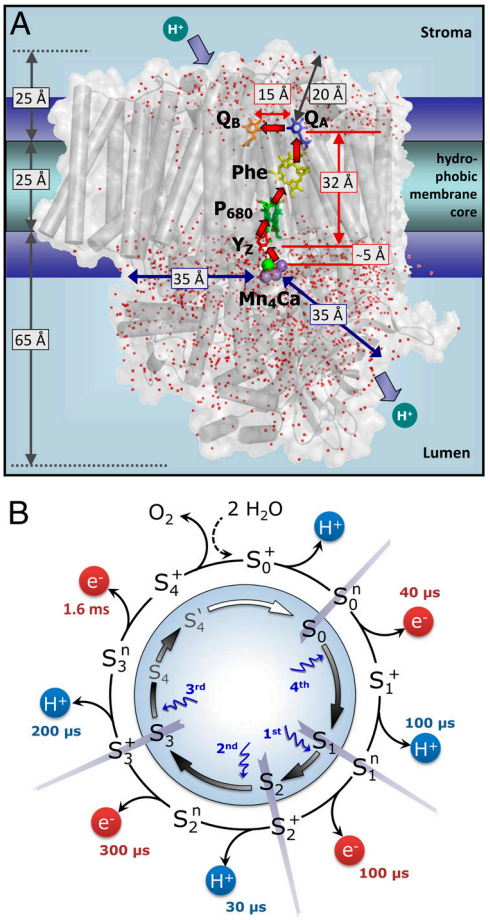

Fig. 1. Photosystem II (*A*) and reaction cycle of water oxidation (*B*). In *A*, crucial redox cofactors and dimensions of the PSII complex are shown (15). Red arrows connect redox cofactors of the ET chain, including the primary electron donor (P_{680}), the primary pheophytin acceptor (Phe), the primary (Q_A) and secondary (Q_B) quinone acceptors, and, at the electron donor side, a redox-active tyrosine (Y_Z) and the Mn complex. Water molecules resolved in the crystallographic model (Protein Data Bank entry 3ARC; ref. 15) are shown as red dots; the indicated distances illustrate relevant dimensions. In *B*, the classical Kok model (16) (inner circle, including states S_4 and S_4'; ref. 22) is extended to describe both oxidation of the Mn complex by ET to the Y_Z radical and proton removal from the Mn complex or its ligand environment by long-distance proton transfer. Coupling of the ET step to local proton shifts is not covered by the shown framework model. The subscripts indicate the number of oxidation equivalents accumulated at the Mn complex; the superscripts indicate the charge relative to the dark-stable S_1-state (+, positive; *n*, neutral). The proton release steps in the $S_0 \rightarrow S_1$ and $S_2 \rightarrow S_3$ transitions have not been tracked in time-resolved experiments before, but now these steps are detected in the PBD experiments; the indicated time constants result from the present study.

about 2 $Å^3$ per PSII. For comparison, the average volume of one water molecule in aqueous solution is approximately 30 $Å^3$. In photoacoustic or photothermal measurements, it is usually found that a volume contraction results from the (light-induced) deposition of charges at the electron donor and/or acceptor, as has been shown for synthetic molecules (39, 40) and photosystems (41, 42). Also in PSII, the light-induced formation of the primary quinone acceptor (Q_A^-) and of $Y_Z^{ox(+)}$ is associated with a volume contraction (37, 43). The decharging of the donor side by removal of a proton results in an expansion that reverts the $Y_Z^{ox(+)}$ contribution to the preceding contraction. This enables monitoring of proton removal from the Mn complex by measuring the concomitant volume expansion in the PBD experiment, thereby revealing the temporal sequence of electron and proton removal steps in the classical $S_0 \rightarrow S_1$ and $S_2 \rightarrow S_3$ transitions.

Results

For insight into the individual *S*-state transitions, PBD measurements were combined with the following laser-flash protocol (Fig. S1): Dark-adapted PSII membrane particles were excited by a sequence of *n* saturating ns-laser flashes (532 nm, 10 mJ cm^{-2}). Each flash populated predominantly a specific stable/semistable *S*-state of Kok's classical reaction cycle (16, 17), namely S_1 ($n = 0$, dark-adapted PSII), S_2 ($n = 1$), S_3 ($n = 2$), S_0 ($n = 3$), and again S_1 ($n = 4$). Subsequently, a single subsaturating ns-flash (0.1 mJ cm^{-2}) was applied and the PBD signal induced thereby was recorded. The subsaturating flash initiated predominantly the following transitions: $S_1 \rightarrow S_2$ (flash 1), $S_2 \rightarrow S_3$ (flash 2), $S_3 \rightarrow S_0$ (flash 3), and $S_0 \rightarrow S_1$ (flash 4). The measured PBD signals were corrected for imperfect advancement in the *S*-state cycle (*S*-state mixing) using previously established procedures (26, 44) (Fig. S2). We note that all central conclusions of this work are independent of the details of the correction procedure. Corrected PBD transients for each of the four transitions between semistable *S*-states are shown in Fig. 2 and discussed below.

The instantaneous rise observed after each flash (at 25 °C) is attributable to the rapid light-induced processes that result in reduction of Q_A and oxidation of the tyrosine donor ($Y_Z^{ox(+)}$ formation) (12). At 12 °C, the magnitude of the instantaneous rise was smaller than at 25 °C, and at 1 °C a decay was observed (Fig. 2*B*). This behavior results from the temperature-dependent thermal (ΔQ) and temperature-independent nonthermal (ΔV) contributions to the PBD signal (34–36) associated with the $Y_Z^{ox(+)}$ Q_A^- formation. Evaluation of the temperature dependence of the rapid phase in comparison to a calorimetric standard (Figs. S3–S5) yielded an apparent volume contraction (ΔV) by about −12 $Å^3$, in reasonable agreement with previous estimates (37, 43). For a possible contribution to the PBD signals associated with interquinone electron transfer, see Figs. S6 and S7 and Table S1. [We note that no ΔV values presented herein were cor-

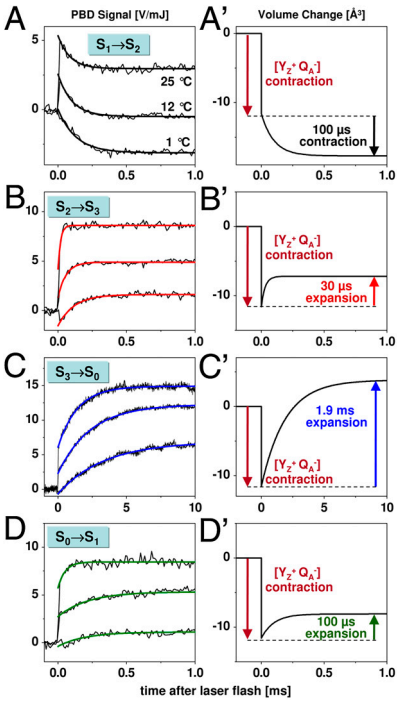

Fig. 2. Flash-induced PBD signals and volume changes: $S_1 \rightarrow S_2$ (*A*, *A'*), $S_2 \rightarrow S_3$ (*B*, *B'*), $S_3^+ \rightarrow S_0$ (*C*, *C'*), and $S_0 \rightarrow S_1$ (*D*, *D'*). Thin lines, experimental data; thick lines, simulations using a step-shaped function for the rapid jump caused by $Q_A^- Y_Z^+$ formation and single-exponential functions for the slower signal contributions. (*Right*) Schematic illustration of volume changes deduced from the analysis of the temperature dependence of the PBD signals (time constants for about 20 °C; see Fig. 3).

rected for the effective quantum yield, Φ_{eff}, of the light-induced transition, which could be as low as 50% (*SI Text*). This means that the volume changes per PSII complex may be twice as large as the values documented herein.]

In the $S_1 \rightarrow S_2$ transition (flash 1), the instantaneous $Y_Z^{ox(+)} Q_A^-$ signal (<10 μs) was followed by an exponential decay with a time constant of about 100 μs at 20 °C (Figs. 2 and 3, and Table 1). The amplitude of the decay phase depended only weakly on the temperature, suggesting that it mostly originates from a volume change (ΔV) of the PSII sample; its negative amplitude (PBD-signal decrease) indicates a contraction. The weak temperature dependence of the signal magnitude suggests a small contribution to the signal from a positive ΔQ (heat release) (Table 1). The decay became only slightly slower at lower temperatures, and the Arrhenius plot of the rate constants (Fig. 3*B*) revealed a small activation energy (Table 2). From PBD transients measured in D_2O (Fig. 4), a minor H/D kinetic isotope effect (KIE) of 1.3 was determined. (The KIE is the ratio of time constants determined in D_2O or H_2O; $KIE = \tau_D/\tau_H = k_H/k_D$.) Time constant, activation energy, and KIE agree well with figures previously determined for the ET from the Mn complex to Y_Z^{ox} in the $S_1 \rightarrow S_2$ transition (22, 26, 27) (Fig. 1*B*).

The large contraction associated with the ET from the Mn complex to Y_Z^{ox} is specifically observed in the $S_1 \rightarrow S_2$ transition. For $S_2 \rightarrow S_3$, such a contraction paralleling the ET step was not detectable (Fig. 2*B* and Fig. S7). In the $S_0 \rightarrow S_1$ transition, a small contraction might be coupled to the ET step (Fig. S4). We note that the contraction associated with the ET in the $S_1 \rightarrow S_2$ transition, which likely is reversed in the $S_3 \rightarrow S_0$ transition (see below), could reflect an interesting new mode of coupling the ET step to nuclear rearrangements, possibly related to changes in the protein backbone conformation suggested by FTIR data (45).

In the $S_2 \rightarrow S_3$ transition (flash 2), the instantaneous $Y_Z^{ox(+)} Q_A^-$ rise was followed by an exponentially rising phase with a time constant of about 30 μs (at 20 °C; Figs. 2 and 3). This rise was roughly 10 times faster than the ET from the Mn complex to Y_Z^{ox} (30 μs versus 300 μs; Table 2) and is thus assignable to a process that precedes the ET step. Its almost temperature-independent signal amplitude (Fig. 3*A*) indicates that the rising phase originates mostly from a volume expansion (Table 1). A striking feature of the rapid rise was its large KIE of close to 6 (Fig. 4 and Table 2), facilitating the assignment to a process involving proton movements. We emphasize that at all temperatures, and also in D_2O, the apparent volume expansion clearly preceded the $Mn_4Ca \rightarrow Y_Z^{ox}$ ET step (Table 2). Thus, we conclude that in the classical $S_2 \rightarrow S_3$ transition, a proton relocation precedes the ET from the Mn complex to Y_Z^{ox}.

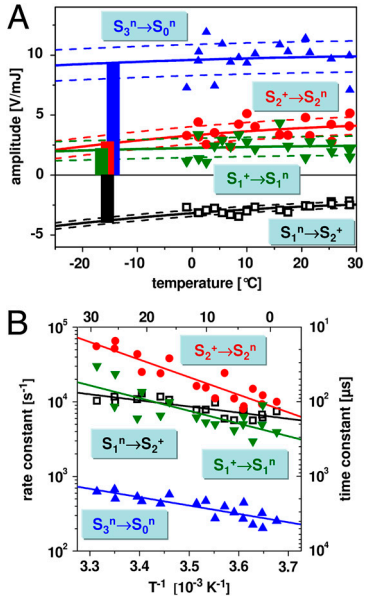

Fig. 3. Temperature dependence of the PBD signals of the four resolved transitions. (*A*) Temperature dependence of the amplitudes as obtained by an exponential simulation (symbols, experimental data; lines obtained by a fit). The dotted lines show the 1σ error ranges of the fit curves. The bars represent the nonthermal part of the PBD signal (volume change ΔV) that corresponds to the PBD amplitude at −14 °C ($T_0 = -14 \pm 1$ °C; *SI Text*). (*B*) Arrhenius plots of the rate constants ($k = \tau^{-1}$, left *y* axis; time constants, τ, on right *y* axis). The symbols indicate the experimentally determined values; the lines are fit curves used for determination of the respective activation energy shown in Table 2.

Table 1. Time constants (τ at 20 °C), volume changes (ΔV), and heat release (ΔQ) of four transitions resolved in PBD measurements

Flash no.	Transition	τ (μs)	ΔV*, † ($Å^3$)	ΔQ † (meV)
1	$S_1^n \rightarrow S_2^+$	98 ± 3	−6.1 ± 0.4	160 ± 50
2	$S_2^+ \rightarrow S_2^n$	29 ± 2	+4.4 ± 1.1	190 ± 120
3	$S_3 \rightarrow S_0$	1,960 ± 90	+15 ± 2.5	60 ± 250
4	$S_1^+ \rightarrow S_1^n$	94 ± 8	+3.5 ± 1.3	40 ± 140

The given parameters were determined from data shown in Fig. 3; error ranges correspond to uncertainty of the fit result at the 1σ level.

*The value of ΔV denotes apparent volume changes calculated using *SI Text*, Eq. **S1**. Negative or positive signs correspond to contractions or expansions, respectively.

†The figures given for ΔV and ΔQ were calculated for a single PSII complex after absorption of one light quantum (without correction for nonunity quantum yield).

In the transition $S_3 \rightarrow S_0 + O_2$ (flash 3), a prominent millisecond rise (τ around 2 ms at 20 °C) that resulted mostly from a volume expansion by about 15 $Å^3$ was visible (Figs. 2 and 3*A*, and Table 1). The moderate activation energy and small KIE of the millisecond phase (Figs. 3 and 4, and Table 2) were similar to the respective values for the ET step ($S_3^n \rightarrow S_4^+$) and the concomitant dioxygen formation ($S_4^+ \rightarrow S_0^+ + O_2$) (26, 27, 46, 47).

Using time-resolved X-ray spectroscopy and near-UV measurements to monitor the oxidation state of the Mn complex, it has been found that an apparent lag phase of an approximately 200-μs duration precedes the millisecond rise of O_2 formation (22, 26, 27, 32). A similar lag phase was not discernable in the PBD transients. Instead, a rising phase with a similar τ value to the previously observed lag phase could be detected by simulation of summed PBD transients (Fig. S5). However, this phase was not sufficiently well-resolved for analysis of its temperature dependence and quantitative determination of ΔQ and ΔV. Conservatively, we conclude that the PBD data are compatible with a volume expansion associated with proton release in the $S_3^+ \rightarrow S_3^n$ transition. Thus, we propose that the overall extent of the expansion in the $S_3 \rightarrow S_0$ transition is explainable by three additive contributions—namely, proton removal from the Mn complex prior to the ET, reversal of the contractions associated with previous manganese oxidation (in the $S_1 \rightarrow S_2$ transition), and removal of a second proton from the Mn complex after the ET (more quantitative considerations appear in *SI Text*).

In the $S_0 \rightarrow S_1$ transition (flash 4), the initial signal increase was followed by an exponentially rising phase with a time constant of approximately 100 μs (at 20 °C). The amplitude of this signal rise was almost temperature-independent, indicating a volume expansion (Fig. 3*A*), similar to the signal rise in the $S_2^+ \rightarrow S_2^n$ transition. Also, further parameters of this phase in the $S_0 \rightarrow S_1$ transition were similar—namely, its large activation energy, its large KIE (approximately 3), and the ΔV magnitude (Tables 1 and 2, and Table S2). The 100-μs rise in the PBD signal was slower than the ET from the Mn complex to Y_Z^{ox} (approximately 40 μs in refs. 22 and 29) (Table 2), implying that the underlying process occurred after the ET step—that is, after the $S_0^n \rightarrow S_1^+$ transition (Fig. 1*B*).

We note that vastly different values have been reported for the ET rate constant of the $S_0 \rightarrow S_1$ transition, ranging from about 40 μs to 300 μs (at approximately 20 °C) (27–29, 32, 48). For the same PSII samples used herein, we have previously determined

Table 2. Kinetic parameters of ET (e^-) and rate-determining proton transfer (PT, H^+) during the reaction cycle of PSII water oxidation at approximately 20 °C

S-state transition		ET/PT	τ (μs)	E_a * (meV)	k_H/k_D
$S_1 \rightarrow S_2$	$S_1^n \rightarrow S_2^+$	e^-	100[†, ‡, §, ¶]	160 ± 30[†, ¶, ‖]	1.3[†], (1.2[‡])
S_2	$S_2^+ \rightarrow S_2^n$	H^+	30[†]	470 ± 50[†]	5.6[†]
$\rightarrow S_3$	$S_2^n \rightarrow S_3^+$	e^-	300[‡, §, ¶, ‖]	*ca.* 360[¶, ‖]	1.7[‡]
S_3	$S_3^+ \rightarrow S_3^n$	H^+	200[‡,§]	180**	2.4 [‡]
	$S_3^n \rightarrow S_0^+$	e^-	*ca.* 1,700[‡,§, ¶, ‖, **, ††, ‡‡]	230 ± 40[†, ‖, ††]	1.3[†], (1.2[‡])
$\rightarrow S_0 + O_2$	$S_0^+ \rightarrow S_0^n$	H^+	-	-	-
S_0	$S_0^n \rightarrow S_1^+$	e^-	40[§, ‡‡]	50[‖]	1.3[¶]
$\rightarrow S_1$	$S_1^+ \rightarrow S_1^n$	H^+	100[†]	340 ± 75[†]	3.0[†]

Kinetic parameters were mostly determined for plant PSII (membrane particles).
*Activation energies (E_a) were derived from the temperature dependence of rate constants (Fig. 3*B*).
[†]PBD results, this work.
[‡]Ref. 26.
[§]Ref. 22.
[¶]Ref. 27.
[‖]Ref. 28.
**Ref. 66; for thermophilic cyanobacteria, ref. 53.
[††]Ref. 46.
[‡‡]Ref. 29.

a value of approximately 40 μs (22), suggesting that the ET step in the $S_0 \rightarrow S_1$ transition is faster than the proton removal step already at room temperature, and even more so at lower temperatures and in D_2O (27, 28). In conclusion, the volume expansion observed in the classical $S_0 \rightarrow S_1$ transition results from a proton relocation (the $S_1^+ \rightarrow S_1^n$ transition in Fig. 1*B*) that takes place after manganese oxidation by ET to Y_Z^{ox}.

Discussion

In the course of the classical $S_2 \rightarrow S_3$ transition, a volume expansion precedes the ET step and can be assigned to the removal of a proton from the Mn complex in the $S_2^+ \rightarrow S_2^n$ transition of the extended *S*-state cycle shown in Fig. 1*B*. This is a central finding of our investigation because it directly supports the proton-first ET in the $S_2 \rightarrow S_3$ transition and establishes a close analogy to the first steps ($S_3^+ \rightarrow S_3^n \rightarrow S_4^+$) in the $S_3 \rightarrow S_0 + O_2$ transition (22). This finding implies that a previously undetected intermediate state (S_2^n) is transiently formed by deprotonation. Why this proton removal step is associated with a volume expansion is explained straightforwardly: The removal of a positive charge (H^+) from the donor side of PSII reverts the preceding volume contraction caused by charging of the donor side by $Y_Z^{ox(+)}$ formation. Detection of this proton removal step ($t_{1/2}$ of only approximately 20 μs at pH 6.2) by analysis of electrochromic absorption changes of the PSII pigments may be feasible, but has not been achieved yet (28, 29, 32), presumably because of technical limitations.

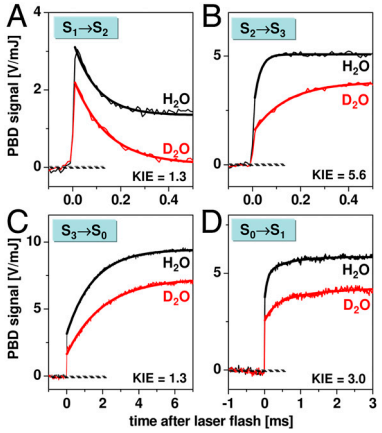

Fig. 4. Comparison of PBD signals on the four *S*-transitions measured for PSII membranes in H_2O (black) and D_2O (red) at 20 °C. Thin lines, experimental data; thick lines, simulations with single-exponential functions plus offset, except for the $S_0 \rightarrow S_1$ transition, for which a double-exponential function plus offset was used (Fig. S7 and Table S2). The respective rate constant ratio is indicated (KIE = k_{H_2O}/k_{D_2O}). The PBD amplitudes differ because of different thermoelastic properties of H_2O and D_2O.

In the course of the classical $S_0 \rightarrow S_1$ transition, a volume expansion occurs after the ET step and is assigned to proton removal from the Mn complex in the $S_1^+ \rightarrow S_1^n$ transition. In analogy to the $S_2^+ \rightarrow S_2^n$ transition, this expansion is explained by removal of a positive charge (H^+) from the donor side of PSII, thereby reversing the contraction caused by $Y_Z^{ox(+)}$ formation. As opposed to the $S_2^+ \rightarrow S_2^n$ transition, the deprotonation in the course of the classical $S_0 \rightarrow S_1$ transition proceeds after oxidation of the Mn complex (after S_1^+ formation). This result directly supports the extended *S*-state cycle scheme (Fig. 1*B*) by revealing transient formation of the S_1^+ intermediate.

The kinetic parameters determined for proton removal from the Mn complex relate to the slowest step in the sequence of all elementary proton transfer steps of the long-distance relocation of a proton from the Mn complex toward the aqueous phase. Presently, the site and physicochemical nature of the rate-determining steps are unknown. We determined similarly large activation energies and KIE values for proton removal from the Y_Z^{ox} S_2^+ and Y_Z^{red} S_1^+ intermediates, pointing to the formation of a transition state of relatively high energy and proton tunneling across a sizeable energetic barrier; a more elaborate analysis of the thermodynamic and kinetic parameters may provide deeper insight (49, 50). Interestingly, activation energy and KIE for proton removal from the Y_Z^{ox} S_3^+ intermediate are smaller, suggesting that site and/or nature of the rate-determining proton transfer may differ. Identification of pathways and modes of proton transfer within PSII could be approached experimentally (e.g., by time-resolved infrared spectroscopy) (51, 52).

In extension of the classical *S*-state cycle model, we have suggested a basic reaction-cycle model (24, 33) that involves nine intermediate states and describes the temporal sequence of light-induced Y_Z oxidation, electron transfer to Y_Z^{ox}, proton removal from the Mn complex, and O_2 formation (Fig. 1*B*). However, with respect to the proton removal steps, the supporting evidence remained largely circumstantial. Only the $S_3^+ \rightarrow S_3^n$ transition (or $S_3 \rightarrow S_4$; ref. 22) had become detectable in time-resolved experiments (22, 26, 27, 32, 53, 54). Now, we have followed the charge-compensating proton removal in the classical $S_0 \rightarrow S_1$ and $S_2 \rightarrow S_3$ transitions and have determined the kinetic parameters of these essential reaction steps (see Table 2).

On these grounds and based on earlier investigations (reviewed in refs. 2 and 24), we propose the basic reactions sequence for the transitions from S_0^n to the S_4^+ state outlined in the following (Figs. 1*B* and 5): (*i*) Starting in the most reduced semistable

S-state, S_0^n, absorption of a photon by PSII induces rapid Y_Z oxidation (<1 μs) followed by ET from the Mn complex to Y_Z^{ox} (40 μs in Fig. 1*B*), resulting in S_1^+ formation. Mn oxidation in the $S_0^n \rightarrow S_1^+$ transition lowers the pK of a Mn ligand, possibly a bridging hydroxide (44, 55, 56), to a value around 3.3 (57). The proton is removed from the Mn complex and relocated toward the lumen only after S_1^+ formation in the $S_1^+ \rightarrow S_1^n$ transition. (*ii*) The next absorbed photon induces Y_Z^{ox} oxidation followed by a $Mn^{III} \rightarrow Mn^{IV}$ oxidation in the $S_1^n \rightarrow S_2^+$ transition. The oxidation of the Mn complex lowers the pK values of ligand groups, but not to an extent sufficient for deprotonation. (*iii*) Oxidation of the Mn complex without any charge-compensating chemical change raises its redox potential to a level that prohibits a second oxidation by Y_Z^{ox} (1, 2, 7). In the S_2^+ state, this redox-potential problem initially prevents oxidation of the Mn complex by Y_Z^{ox}. However, $Y_Z^{ox(+)}$ drives the removal of a proton from the Mn complex, resulting in formation of the S_2^n state within about 30 μs. We propose that the proton is removed from the cluster of water molecules indicated in Fig. 5. Thereby created is a proton vacancy that is effectively delocalized within the water cluster (on the μs time scale), but likely resides mostly on the water molecule close to Y_Z^{ox}, which is coordinated to the Ca ion of the Mn complex. In the subsequent ET step ($S_2^n \rightarrow S_3^+$), $Mn^{III \rightarrow IV}$ oxidation of Mn1 (58–60) is directly coupled to proton transfer to the previously deprotonated water cluster. Such a concerted electron–proton transfer is in line with a comparably large H/D isotope effect for this ET step, and is well-suited to solve the redox-potential problem mentioned above. In the proton removal step preceding the ET, deprotonation of D1–Asp_{61} can be excluded because the $S_2 \rightarrow S_3$ transition is not severely affected in the Asp–Asn mutant (61, 62). A central role of CP43–Arg_{357} (63) is unlikely because this residue is close to neither Y_Z nor Mn1. Thus, we consider deprotonation of the water cluster interconnecting Y_Z and the Mn complex to be the most plausible option, which is supported by the importance of the pK value of the water molecules coordinated to the Ca ion (64). (*iv*) In the $S_3^+ \rightarrow S_3^n \rightarrow S_4^+$ transitions, the basic temporal sequence of proton removal and electron transfer is similar to the one described above for the $S_2^+ \rightarrow S_2^n \rightarrow S_3^+$ transitions. However, the key players are others. As opposed to the $S_2 \rightarrow S_3$ transition, the proton removal step likely involves D1–Asp_{61} (62). Therefore, and in line with the clear differences in H/D isotope effect (KIE) and activation energy (Table 2), we propose that proton removal in the $S_3^+ \rightarrow S_3^n$ transition proceeds along a path that includes D1–Asp_{61} (14, 21), whereas proton removal in the $S_2^+ \rightarrow S_2^n$ transition proceeds along another path starting close to D1–Tyr_{161}/His_{190} (15, 65). In comparison to the ET of the $S_2^n \rightarrow S_3^+$ transition, the $S_3^n \rightarrow S_4^+$ transition may be coupled to more extensive chemical changes suitable to initiate O–O bond formation. Gaining insight into the presently merely hypothetical S_4^+ and S_0^+ intermediates represents a central challenge in future research on photosynthetic water oxidation.

In conclusion, the basic sequence of events in the reaction cycle of water oxidation has now been established for the six transitions leading from S_0^n to S_4^+. This sequence is characterized by the strictly alternating removal of electrons and protons from the Mn complex. Three intermediate states of the catalytic metal center (S_0^+, S_2^n, S_3^n) and its immediate ligand environment are transiently formed. On these grounds, strategies can be developed for characterization of the new reaction intermediates at the atomistic level. The extended *S*-state cycle model (Fig. 1*B*) may serve as a framework for the future design of experimental and theoretical investigations on photosynthetic water oxidation. It may also be worthwhile to scrutinize synthetic systems for catalysis of water oxidation within a conceptual framework that involves redox-potential leveling and local accumulation of four oxidizing equivalents by alternating electron and proton removal from the catalytic site.

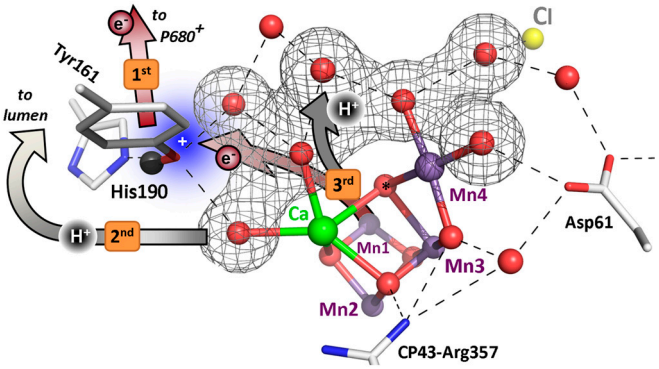

Fig. 5. Sequence of events in the classical $S_2 \rightarrow S_3$ transition of photosynthetic water oxidation. The Mn_4CaO_5 cluster, the redox-active tyrosine (Tyr_{161}), and the key groups of the surrounding hydrogen-bonded network (15) are shown. All indicated amino acid residues are from the D1 subunit of PSII, with exception of CP43–Arg_{357}. (Water molecules, H_xO, are indicated as red spheres; putative H-bonds as broken lines that connect H-bond donor and acceptor. Of all the protons, only the phenolic proton is shown as a grey sphere.) The grey mesh outlines a water cluster that includes 4 H_xO in the first coordination sphere of manganese (Mn4), as well as the calcium (Ca) and three second-sphere water molecules. Within less than 100 ns after absorption of a photon and oxidation of the primary chlorophyll donor of PSII (P680), Tyr_{161} (Y_Z) is oxidized by $P680^+$ ("1st"). Y_Z^{ox} formation results in a rearrangement of the shown H-bonded network (completed within less than 1 μs), likely involving a shift of the phenolic proton to His_{190} and lowering of pK values for deprotonation of the water molecules in the outlined cluster (grey mesh). A proton is removed from the Mn complex/Y_Z environment within about 30 μs, as evidenced by the PBD results presented herein, and a proton vacancy is supposedly created within the outlined water cluster ("2nd"). In the ET to Y_Z^{ox} (about 300 μs), Mn oxidation is directly coupled to a proton transfer step involving the previously created proton vacancy of the water cluster (concerted electron–proton transfer) ("3rd").

Materials and Methods

PSII membrane particles prepared from spinach were resuspended in a buffered solution (80 μg chlorophyll per mL; pH/pD of 6.2), and 20 μM of 2,6-dichloro-*p*-benzoquinone (DCBQ) were added as artificial electron acceptor. The PBD experiments were carried out and analyzed as described previously (37, 38). In the PBD experiments presented herein, 100 mL of PSII suspension were kept in a dark reservoir on ice (gently stirred) and pumped first through a thermostated laboratory-built heat exchanger and then into the sample compartment of the thermostated flow-through cuvette (3-mm optical path). Then, the respective laser-flash protocol was applied (0–4 saturating ns-laser flashes plus a single subsaturating flash; 532 nm; see Fig. S1). The PBD signal induced by the nonsaturating laser flash was recorded. In the next pump cycle, the flow-through cuvette was filled again with a fresh sample of dark-adapted PSII. Extensive signal averaging was applied; about 4,000 measurements were needed for obtaining the data in Fig. 2 (*SI Text*).

ACKNOWLEDGMENTS. We thank M. Fünning for preparation of the PSII membrane particles. We acknowledge support from the Berlin Cluster of Excellence on Unifying Concepts in Catalysis (UniCat), the European Union (7th Framework Program; *SOLAR-H2* consortium, Grant 212508), the German "Bundesministerium für Bildung und Forschung" (BMBF; H_2 *Design Cell* consortium, Grant 03SF0355D), and the Volkswagen Foundation (Grant I/77-575). M.H. thanks the Deutsche Forschungsgemeinschaft for a Heisenberg fellowship.

1. McEvoy JP, Brudvig GW (2006) Water-splitting chemistry of photosystem II. *Chem Rev* 106:4455–4483.
2. Dau H, Haumann M (2008) The manganese complex of photosystem II in its reaction cycle: Basic framework and possible realization at the atomic level. *Coord Chem Rev* 252:273–295.
3. Barber J (2009) Photosynthetic energy conversion: Natural and artificial. *Chem Soc Rev* 38:185–196.
4. Blankenship RE (2002) *Molecular Mechanisms of Photosynthesis* (Blackwell Science, Oxford).

5. Rutherford AW, Moore TA (2008) Mimicking photosynthesis, but just the best bits. *Nature* 453:449.
6. Magnuson A, et al. (2009) Biomimetic and microbial approaches to solar fuel generation. *Acc Chem Res* 42:1899–1909.
7. Dau H, et al. (2010) The mechanism of water oxidation: From electrolysis via homogeneous to biological catalysis. *ChemCatChem* 2:724–761.
8. Lubitz W, Reijerse EJ, Messinger J (2008) Solar water-splitting into H_2 and O_2: Design principles of photosystem II and hydrogenases. *Energy Environ Sci* 1:15–31.
9. Dau H, Zaharieva I (2009) Principles, efficiency, and blueprint character of solar-energy conversion in photosynthetic water oxidation. *Acc Chem Res* 42:1861–1870.
10. Barry BA, Babcock GT (1987) Tyrosine radicals are involved in the photosynthetic oxygen-evolving system. *Proc Natl Acad Sci USA* 84:7099–7103.
11. Styring S, Sjöholm J, Mamedov F (2012) Two tyrosines that changed the world: Interfacing the oxidizing power of photochemistry to water splitting in photosystem II. *Biochim Biophys Acta* 1817:76–87.
12. Rappaport F, Diner BA (2008) Primary photochemistry and energetics leading to the oxidation of the $(Mn)_4Ca$ cluster and to the evolution of molecular oxygen in photosystem II. *Coord Chem Rev* 252:259–272.
13. Zouni A, et al. (2001) Crystal structure of photosystem II from *Synechococcus elongatus* at 3.8 Å resolution. *Nature* 409:739–743.
14. Ferreira KN, Iverson TM, Maghlaoui K, Barber J, Iwata S (2004) Architecture of the photosynthetic oxygen-evolving center. *Science* 303:1831–1838.
15. Umena Y, Kawakami K, Shen J-R, Kamiya N (2011) Crystal structure of oxygen-evolving photosystem II at a resolution of 1.9 Å. *Nature* 473:55–60.
16. Kok B, Forbush B, McGloin M (1970) Cooperation of charges in photosynthetic O_2 evolution, I. A linear four-step mechanism. *Photochem Photobiol* 11:457–475.
17. Dau H, Haumann M (2007) Time-resolved X-ray spectroscopy leads to an extension of the classical *S*-state cycle model of photosynthetic oxygen evolution. *Photosynth Res* 92:327–343.
18. Lavergne J, Junge W (1993) Proton release during the redox cycle of the water oxidase. *Photosynth Res* 38:279–296.
19. Junge W, Haumann M, Ahlbrink R, Mulkidjanian A, Clausen J (2002) Electrostatics and proton transfer in photosynthetic water oxidation. *Philos Trans R Soc Lond B Biol Sci* 357:1407–1418.
20. Rappaport F, Lavergne J (1991) Proton release during successive oxidation steps of the photosynthetic water oxidation process: Stoichiometries and pH dependence. *Biochemistry* 30:10004–10012.
21. Ho FM (2008) Uncovering channels in photosystem II by computer modelling: Current progress, future prospects, and lessons from analogous systems. *Photosynth Res* 98:503–522.
22. Haumann M, et al. (2005) Photosynthetic O_2 formation tracked by time-resolved X-ray experiments. *Science* 310:1019–1021.
23. Hoganson CW, Babcock GT (1997) A metalloradical mechanism for the generation of oxygen from water in photosynthesis. *Science* 277:1953–1956.
24. Dau H, Haumann M (2007) Eight steps preceding O—O bond formation in oxygenic photosynthesis: A basic reaction cycle of the photosystem II manganese complex. *Biochim Biophys Acta* 1767:472–483.
25. Meyer TJ, Huynh MHV, Thorp HH (2007) The possible role of proton-coupled electron transfer (PCET) in water oxidation by photosystem II. *Angew Chem Int Ed* 46:5284–5304.
26. Gerencsér L, Dau H (2010) Water oxidation by photosystem II: H_2O–D_2O exchange and the influence of pH support formation of an intermediate by removal of a proton before dioxygen creation. *Biochemistry* 49:10098–10106.
27. Haumann M, Bögershausen O, Cherepanov D, Ahlbrink R, Junge W (1997) Photosynthetic oxygen evolution: H/D isotope effects and the coupling between electron and proton transfer during the redox reactions at the oxidizing side of photosystem II. *Photosynth Res* 51:193–208.
28. Renger G, Hanssum B (1992) Studies on the reaction coordinates of the water oxidase in PS II membrane fragments from spinach. *FEBS Lett* 299:28–32.
29. Dekker JP, Plijter JJ, Ouwehand L, van Gorkom HJ (1984) Kinetics of manganese redox transitions in the oxygen evolving apparatus of photosynthesis. *Biochim Biophys Acta* 767:176–179.
30. Haumann M, Junge W (1994) Extent and rate of proton release by photosynthetic water oxidation in thylakoids: Electrostatic relaxation versus chemical production. *Biochemistry* 33:864–872.
31. Schlodder E, Witt HT (1999) Stoichiometry of proton release from the catalytic center in photosynthetic water oxidation. Reexamination by a glass electrode study at ph 5.5–7. *J Biol Chem* 274:30387–30392.
32. Rappaport F, Blanchard-Desce M, Lavergne J (1994) Kinetics of electron transfer and electrochromic change during the redox transition of the photosynthetic oxygen-evolving complex. *Biochim Biophys Acta* 1184:178–192.
33. Dau H, Haumann M (2006) Reaction cycle of photosynthetic water oxidation in plants and cyanobacteria (response letter). *Science* 312:1471–1472.
34. Braslavsky SE, Heibel GE (1992) Time-resolved photothermal and photoacoustic methods applied to photoinduced processes in solution. *Chem Rev* 92:1381–1410.
35. Falvey DE (1997) Photothermal beam deflection calorimetry in solution photochemistry: Recent progress and future prospects. *Photochem Photobiol* 65:4–9.
36. Gensch T, Viappiani C (2003) Time-resolved photothermal methods: Accessing time-resolved thermodynamics of photoinduced processes in chemistry and biology. *Photochem Photobiol Sci* 2:699–721.
37. Krivanek R, Dau H, Haumann M (2008) Enthalpy changes during photosynthetic water oxidation tracked by time-resolved calorimetry using a photothermal beam deflection technique. *Biophys J* 94:1890–1903.
38. Klauss A, Krivanek R, Dau H, Haumann M (2009) Energetics and kinetics of photosynthetic water oxidation studied by photothermal beam deflection (PBD) experiments. *Photosynth Res* 102:499–509.
39. Feitelson J, Mauzerall D (2002) Enthalpy and electrostriction in the electron-transfer reaction between triplet zinc uroporphyrin and ferricyanide. *J Phys Chem B* 106:9674–9678.
40. Rizzi AC, et al. (2008) Entropic changes control the charge separation process in triads mimicking photosynthetic charge separation. *J Phys Chem A* 112:4215–4223.
41. Hou HJM, Mauzerall D (2011) Listening to PS II: Enthalpy, entropy, and volume changes. *J Photochem Photobiol B* 104:357–365.
42. Mauzerall D, Hou JM, Boichenko VA (2002) Volume changes and electrostriction in the primary photoreactions of various photosynthetic systems: Estimation of dielectric coefficient in bacterial reaction centers and of the observed volume changes with the Drude–Nernst equation. *Photosynth Res* 74:173–180.
43. Hou JM, Boichenko VA, Diner BA, Mauzerall D (2001) Thermodynamics of electron transfer in oxygenic photosynthetic reaction centers: Volume change, enthalpy, and entropy of electron-transfer reactions in manganese-depleted photosystem II core complexes. *Biochemistry* 40:7117–7125.
44. Haumann M, et al. (2005) Structural and oxidation state changes of the photosystem II manganese complex in four transitions of the water oxidation cycle ($S_0 \rightarrow S_1$, $S_1 \rightarrow S_2$, $S_2 \rightarrow S_3$, and $S_{3,4} \rightarrow S_0$) characterized by X-ray absorption spectroscopy at 20 K and room temperature. *Biochemistry* 44:1894–1908.
45. Noguchi T (2008) Fourier transform infrared analysis of the photosynthetic oxygen-evolving center. *Coord Chem Rev* 252:336–346.
46. Buchta J, Grabolle M, Dau H (2007) Photosynthetic dioxygen formation studied by time-resolved delayed fluorescence measurements: Method, rationale, and results on the activation energy of dioxygen formation. *Biochim Biophys Acta* 1767:565–574.
47. Karge M, Irrgang KD, Renger G (1997) Analysis of the reaction coordinate of photosynthetic water oxidation by kinetic measurements of 355 nm absorption changes at different temperatures in photosystem II preparations suspended in either H_2O or D_2O. *Biochemistry* 36:8904–8913.
48. Razeghifard MR, Klughammer C, Pace RJ (1997) Electron paramagnetic resonance kinetic studies of the *S* states in spinach thylakoids. *Biochemistry* 36:86–92.
49. Hatcher E, Soudackov A, Hammes-Schiffer S (2005) Comparison of dynamical aspects of nonadiabatic electron, proton, and proton-coupled electron transfer reactions. *Chem Phys* 319:93–100.
50. Krishtalik LI (2000) The mechanism of the proton transfer: An outline. *Biochim Biophys Acta* 1458:6–27.
51. Garczarek F, Gerwert K (2006) Functional waters in intraprotein proton transfer monitored by FTIR difference spectroscopy. *Nature* 439:109–112.
52. Barry BA, et al. (2006) Time-resolved vibrational spectroscopy detects protein-based intermediates in the photosynthetic oxygen-evolving cycle. *Proc Natl Acad Sci USA* 103:7288–7291.
53. Rappaport F, Ishida N, Sugiura M, Boussac A (2011) Ca^{2+} determines the entropy changes associated with the formation of transition states during water oxidation by photosystem II. *Energy Environ Sci* 4:2520–2524.
54. Razeghifard MR, Pace RJ (1999) EPR kinetic studies of oxygen release in thylakoids and PSII membranes: An intermediate in the S_3 to S_0 transition. *Biochemistry* 38:1252–1257.
55. Dau H, Iuzzolino L, Dittmer J (2001) The tetra-manganese complex of photosystem II during its redox cycle: X-ray absorption results and mechanistic implications. *Biochim Biophys Acta* 1503:24–39.
56. Robblee JH, et al. (2002) The Mn cluster in the S_0 state of the oxygen-evolving complex of photosystem II studied by EXAFS spectroscopy: Are there three di-μ-oxo-bridged Mn_2 moieties in the tetranuclear Mn complex? *J Am Chem Soc* 124:7459–7471.
57. Zaharieva I, Wichmann JM, Dau H (2011) Thermodynamic limitations of photosynthetic water oxidation at high proton concentrations. *J Biol Chem* 286:18222–18228.
58. Teutloff C, et al. (2009) Electronic structure of the tyrosine D radical and the water-splitting complex from pulsed ENDOR spectroscopy on photosystem II single crystals. *Phys Chem Chem Phys* 11:6715–6726.
59. Siegbahn PE (2008) A structure-consistent mechanism for dioxygen formation in photosystem II. *Chem Eur J* 14:8290–8302.
60. Ames W, et al. (2011) Theoretical evaluation of structural models of the S_2 state in the oxygen evolving complex of photosystem II: Protonation states and magnetic interactions. *J Am Chem Soc* 133:19743–19757.
61. Hundelt M, Hays AM, Debus RJ, Junge W (1998) Oxygenic photosystem II: The mutation D1–D61N in Synechocystis sp. PCC 6803 retards *S*-state transitions without affecting electron transfer from Y_Z to $P680^+$. *Biochemistry* 37:14450–14456.
62. Dilbeck PL, et al. (2012) The mutation D1–D61N in Synechocystis sp. PCC 6803 allows the observation of pH-sensitive intermediates in the formation and release of O_2 from photosystem II. *Biochemistry* 51:1079–1091.
63. McEvoy JP, Brudvig GW (2004) Structure-based mechanism of photosynthetic water oxidation. *Phys Chem Chem Phys* 6:4754–4763.
64. Vrettos JS, Stone DA, Brudvig GW (2001) Quantifying the ion selectivity of the Ca^{2+} site in photosystem II: Evidence for direct involvement of Ca^{2+} in O_2 formation. *Biochemistry* 40:7937–7945.
65. Bondar AN, Dau H (2012) Extended protein/water H-bond networks in photosynthetic water oxidation. *Biochim Biophys Acta* 1817:1177–1190.
66. Zaharieva I, Grabolle M, Chernev P, Dau H (2013) Water oxidation in photosystem II: Energetics and kinetics of intermediates formation in $S_2 \rightarrow S_3$ and $S_3 \rightarrow S_0$ transitions monitored by delayed chlorophyll fluorescence. *Proceedings of the Fifteenth International Conference on Photosynthesis*, in press.